The Astrophysical Journal, 977:103 (15pp), 2024 December 10 https://doi.org/10.3847/1538-4357/ad89a7

Confirming the Tidal Tails of the Young Open Cluster Blanco 1 with TESS Rotation Periods

Lizhou Sha[1], Andrew M. Vanderburg[2], Luke G. Bouma[3], and Chelsea X. Huang[4]
[1] Department of Astronomy, University of Wisconsin–Madison, 475 N Charter St, Madison, WI 53706, USA; lsha@wisc.edu
[2] Department of Physics and Kavli Institute for Astrophysics and Space Research, Massachusetts Institute of Technology, Cambridge, MA 02139, USA
[3] Department of Astronomy, California Institute of Technology, Pasadena, CA 91125, USA
[4] Centre for Astrophysics, University of Southern Queensland, Toowoomba, Queensland 4350, Australia
Received 2024 April 17; revised 2024 August 29; accepted 2024 September 5; published 2024 December 5

Abstract

Blanco 1 is an ≈130 Myr open cluster located 240 pc from the Sun, below the Galactic plane. Recent studies have reported the existence of diffuse tidal tails extending 50–60 pc from the cluster center based on the positions and velocities measured by Gaia. To independently assess the reality and extent of this structure, we used light curves generated from TESS full-frame images to search for photometric rotation periods of stars in and around Blanco 1. We detected rotation periods down to a stellar effective temperature of ≈3100 K in 347 of the 603 cluster member candidates for which we have light curves. For cluster members in the core and candidate members in the tidal tails, both within a temperature range of 4400–6200 K, 74% and 72% of the rotation periods, respectively, are consistent with the single-star gyrochronological sequence. In contrast, a comparison sample of field stars yielded gyrochrone-consistent rotation periods for only 8.5% of the stars. The tidal tail candidates' overall conformance to the core members' gyrochrone sequence implies that their contamination ratio is consistent with zero and <0.33 at the 2σ level. This result confirms the existence of Blanco 1 tidal tails and doubles the number of Blanco 1 members for which there are both spatio-kinematic and rotation-based cluster membership verification. Extending the strategy of using TESS light curves for gyrochronology to other nearby young open clusters and stellar associations may provide a viable strategy for mapping out their dissolution and broadening the search for young exoplanets.

Unified Astronomy Thesaurus concepts: Open star clusters (1160); Tidal tails (1701); Stellar photometry (1620); Stellar rotation (1629); Stellar ages (1581)

Materials only available in the online version of record: machine-readable tables

1. Introduction

The abundance of precise astrometric, kinematic, and photometric data brought to us by the Gaia mission (Gaia Collaboration et al. 2016) has ushered in a new age of knowledge in stellar clusters and associations. With discoveries like the Gaia–Enceladus sausage (V. Belokurov et al. 2018), the Theia groups (M. Kounkel & K. Covey 2019; J. Gagné et al. 2021), and tidal tails or coronae of open clusters (T. Cantat-Gaudin et al. 2018; S. Meingast et al. 2021), Gaia has enriched our story of Galactic structure. Given the Gaia Data Release 3 (DR3) completeness down to a magnitude of $G = 20.7$ (S. T. Hodgkin et al. 2021), we can leverage its data to trace the dissolution of clusters spanning a large portion of the sky. This all-sky coverage is critical because stars form bound and embedded in their primordial molecular clouds, but as they turn on and disperse the clouds, the cluster becomes "open" and dissolves over a typical timescale of 10–100 Myr (C. J. Lada & E. A. Lada 2003; M. R. Krumholz et al. 2019). Thus, by leveraging Gaia's extreme precision and all-sky coverage, we are gaining a much more complete picture of diffuse structures like stellar associations and tidal tails of open clusters than previously possible.

While Gaia's ability to detect diffuse structures is revolutionizing the understanding of our Galaxy, studying these objects poses unique challenges. In particular, because these diffuse structures span significantly larger volumes in the Galaxy than compact structures like open clusters, the probability that field stars can mimic the kinematic and color–magnitude signatures of association members increases greatly. Thus, Gaia data alone are often not sufficient for validating membership. This problem is exacerbated by different clustering algorithms, such as hierarchical density-based clustering (e.g., HDBSCAN) or Gaussian mixture models, often yielding different extents for these associations (E. L. Hunt & S. Reffert 2021). As a result, we have to rely on additional age proxies, such as stellar spin down due to magnetic braking, lithium depletion boundary, and coronal X-ray emission, to verify membership (see D. R. Soderblom et al. 2014 for a review).

Meanwhile, advances in high-cadence photometric surveys have made using stellar rotation as a proxy for age, a practice known as gyrochronology (S. A. Barnes 2003), an attractive observational strategy. Gyrochronology studies of clusters and associations and exoplanet transit surveys both benefit from uninterrupted monitoring of a wide area of the sky, a strategy pioneered by the Monitor project (S. Aigrain et al. 2007; J. Irwin et al. 2009). After early successes from ground-based transit surveys such as HATNet (J. D. Hartman et al. 2010) and SuperWASP (P. Delorme et al. 2011) and the space-based Kepler mission (S. Meibom et al. 2011), this strategy matured by the K2 mission and was used to study the Pleiades (L. M. Rebull et al. 2016), Hyades (S. T. Douglas et al. 2016),

and M67 (S. A. Barnes et al. 2016; R. Esselstein et al. 2018) clusters. As the successor to Kepler, the Transiting Exoplanet Survey Satellite (TESS; G. R. Ricker et al. 2015) trades off spatial resolution for a much wider field of view, allowing us to efficiently apply gyrochronology to larger and more diffuse structures. To wit, J. L. Curtis et al. (2019) verified the existence of the Pisces–Eridanus stream (S. Meingast et al. 2019) and found it to have the same age as the Pleiades. Later studies have verified the tidal tails around NGC 2516 (L. G. Bouma et al. 2021) and a diffuse complex of stars in the α Persei cluster (A. W. Boyle & L. G. Bouma 2023). Furthermore, the search for young planets in TESS and Kepler data has also led to the discovery of new young stellar associations (B. M. Tofflemire et al. 2021; M. G. Barber et al. 2022; E. R. Newton et al. 2022).

It is in light of the expanded cluster membership knowledge in the wake of Gaia and the precise photometry over a large field of view by TESS that we revisit rotation periods in the open cluster Blanco 1. This nearby (≈240 pc; X. Pang et al. 2021) and young (≈130 Myr; P. A. Cargile et al. 2010) cluster has been extensively studied through photometry, spectroscopy, and astrometry in the 75 yr since its discovery by V. M. Blanco (1949). The first ground-based transit survey to study Blanco 1 was Kilodegree Extremely Little Telescope–South (J. Pepper et al. 2008, 2012), which monitored 33 stars for 43 nights spread over 90 days and detected periods for 23 of them (P. A. Cargile et al. 2014). Since Gaia Data Release 2 (DR2), the Next Generation Transit Survey had monitored 170 stars for ≈200 nights and detected periods for 127 (E. Gillen et al. 2020). After those surveys had been published, several authors reported on Blanco 1's extended structure, variously known as "coronae" or "tidal tails" (Y. Zhang et al. 2020; S. Meingast et al. 2021; X. Pang et al. 2021). Leveraging these expanded member lists, we aim to extend these earlier rotation period studies to stars in Blanco 1's tidal tails and, for the first time, independently verify that their ages are consistent with stars in the cluster core.

This paper is organized as follows. We begin by detailing our procedure for selecting candidate members of Blanco 1 and a matched comparison sample of field stars for experimental control in Section 2. After briefly explaining how we generated the TESS light curves in Section 3, we describe our method for measuring rotation periods in Section 4. These measurements result (Section 5) in a stellar effective temperature–rotation period relation for Blanco 1 that contains the tidal tail candidates for the first time, and we use this relation to estimate the field star contamination rate in the tidal tails. Finally, in Section 6, we round off this paper by discussing the implications of the verified tidal tails, both for the morphology of Blanco 1 and the possibility of extending this observational strategy to other nearby young open clusters, focusing on the prospect for enhancing the local young star census and the search for young exoplanets.

2. Selecting Cluster Candidates and a Comparison Sample

2.1. Selecting a Candidate List of Blanco 1 Members

In selecting a candidate list of Blanco 1 membership for this paper, we focused on those produced in recent years based on Gaia DR2 or Extended (E)DR3 data. Together with the Gaia DR2 catalog (Gaia Collaboration et al. 2018b),

	G18	CG18	Z20	M21	P21	T22	H22	A23
G18	489	354	425	390	433	342	346	405
CG18	354	381	368	330	370	354	367	343
Z20	425	368	644	485	605	467	390	459
M21	390	330	485	494	476	392	329	390
P21	433	370	605	476	703	485	396	485
T22	342	354	467	392	485	529	371	374
H22	346	367	390	329	396	371	408	360
A23	405	343	459	390	485	374	360	488

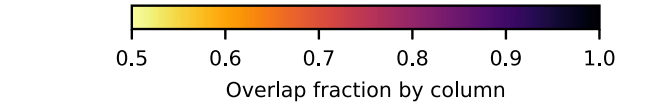

Figure 1. A table summarizing the degree to which eight literature references are in agreement over Blanco 1 candidates. Each row and column represent one of eight references that contain membership lists for Blanco 1 compiled using Gaia DR2 or (E)DR3 data. The number in each cell is the number of candidates shared by that row's and column's references. The color in each cell indicate the fraction of common candidates with respect to the total number identified by each column's reference. References: G18: Gaia Collaboration et al. (2018a); CG18: T. Cantat-Gaudin et al. (2018); Z20: Y. Zhang et al. (2020); M21: S. Meingast et al. (2021); P21: X. Pang et al. (2021); T22: Y. Tarricq et al. (2022); H22: Z. He et al. (2022); and A23: J. Alfonso & A. García-Varela (2023).

Gaia Collaboration et al. (2018a) released a list of 489 Blanco 1 candidates based on astrometry. Using the unsupervised UPMASK algorithm, T. Cantat-Gaudin et al. (2018) found 381 candidates with membership probabilities over 50%. Still using Gaia DR2 but with a larger search radius of 100 pc, Y. Zhang et al. (2020) identified the tidal tail structure of Blanco 1 for the first time with the unsupervised machine learning algorithm STARGO, listing 644 candidates. S. Meingast et al. (2021) confirmed the existence of the tidal tails (which they called "coronae") and listed 494 candidates, taking into account cluster bulk velocities and correcting for line-of-sight distance errors. Taking advantage of the higher astrometric precision of Gaia EDR3, X. Pang et al. (2021) used STARGO to find 703 candidates, the most thus far. The most recent membership lists produced with Gaia (E)DR3 largely confirmed the earlier findings of the tidal tails, with the number of cluster candidates ranging 408–529 (Z. He et al. 2022; Y. Tarricq et al. 2022; J. Alfonso & A. García-Varela 2023).

We chose to adopt the membership list of X. Pang et al. (2021) rather than attempting to synthesize a superset of all available literature references. We found their list to be the most complete, encompassing 85% of the 829 distinct candidates in the literature. Further, almost 95% of the 703 candidates identified by X. Pang et al. (2021) also appear in at least another reference, whereas out of the 126 candidates not found on their list, over 75% only appear in one reference. This high degree of overlap is visible in Figure 1 as distinctly dark colors in the corresponding row labeled P21, indicating that virtually all candidates found by X. Pang et al. (2021) are also identified by the authors corresponding to each column, suggesting that their list has a low false positive rate. For the sake of consistency and uniformity in selection criterion, we adopt the 703 candidates of X. Pang et al. (2021) for further analysis in the paper. Figure 2 shows a chart of these candidates on the sky.

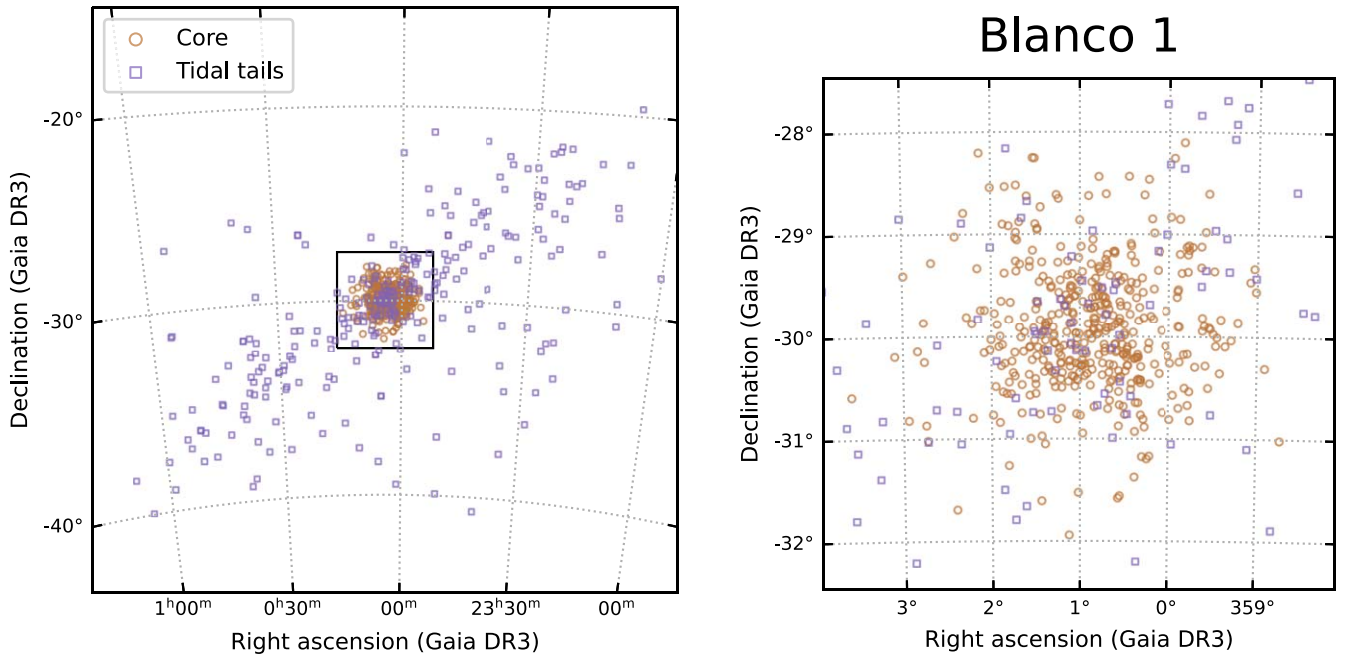

Figure 2. Sky charts for Blanco 1 cluster candidate members identified by X. Pang et al. (2021). The charted positions are from Gaia DR3. Left: full view of Blanco 1. Right: zoomed-in view of the cluster core. The circular orange marks are the stars within the tidal radius of the cluster, and the square magenta marks are those outside of the tidal radius.

2.2. Stellar Multiplicity

As we would like to use stellar rotation periods to verify cluster membership, we need to identify binary stars in the sample. In the same cluster, binary stars often rotate faster than single stars due to various mechanisms that inhibit angular momentum loss (S. Meibom et al. 2007). In addition, they may be eclipsing binaries or show ellipsoidal variations that may be confused with a rotational signal. Here, we use the Gaia DR3 to systematically identify astrometric, spectroscopic, and photometric binaries. As detailed in the following paragraphs, we adopted three simple criteria for stellar multiplicity:

1. excess astrometric uncertainty: Renormalized Unit Weight Error (RUWE) > 1.2,
2. excess radial velocity (RV) uncertainty, and
3. location in the binary sequence on the Hertzsprung–Russell (H-R) diagram.

Any candidate that satisfies any one of these criteria is deemed a likely multiple star for our analysis.

We identified astrometric binaries by the excess uncertainty in their Gaia DR3 astrometric solution. This excess uncertainty is parameterized by the unit-less RUWE parameter, which is expected to be close to one for "well-behaved" single sources (L. Lindegren et al. 2021). Based on the empirical distribution of RUWE of the Blanco 1 candidates (Figure 3, top panel), we chose a cutoff of

$$\mathrm{RUWE} > 1.2, \tag{1}$$

for multiplicity. Sources that satisfied this condition have the `multi_ruwe_flag` set to `True` in Tables 1 and 2.

We used Gaia DR3 RV uncertainties to identify spectroscopic binaries, whenever Gaia DR3 RV measurements were available. Based on the empirical dependence of RV uncertainty with photometric magnitude (Figure 3, middle panel), we used a hand-tuned multiplicity cutoff in the form of

$$\frac{\sigma_{\mathrm{RV}}}{\mathrm{km\ s^{-1}}} > 4.8 + 0.02\,(G-8)^2 + 0.002\,(G-8)^4, \tag{2}$$

where G is the Gaia G magnitude of the star. Sources that satisfied this condition have the `multi_rv_flag` set to `True` in Tables 1 and 2.

Finally, we used the H-R diagram to identify Blanco 1 stars on the binary sequence. The H-R diagram (Figure 4) was constructed using Gaia DR3 $G_{\mathrm{BP}} - G_{\mathrm{RP}}$ color and G magnitudes, which were converted to absolute magnitudes using the corrected distances from X. Pang et al. (2021). We fitted a ninth-order polynomial to the main sequence of Blanco 1 (see Appendix B for details). We deemed any stars with $G_{\mathrm{BP}} - G_{\mathrm{RP}} < 2.8$ and more than 0.3 mag brighter than the main sequence as predicted by the ninth-order polynomial to be part of the binary sequence (Figure 3, bottom panel). The additional constraint on color was to exclude M dwarfs that might not have converged on the zero-age main sequence at the age of Blanco 1. Blanco 1 stars deemed to be on the binary sequence had their `multi_hr_flag` set to `True` in Table 1. As the comparison sample stars were not expected to be on the same isochrone, we did not check them for the possibility of photometric binaries.

Altogether, 100 sources in the Blanco 1 candidate list from X. Pang et al. (2021) were marked as binaries. Out of those, 67, 17, and 46 sources were marked according to at least one of the RUWE, RV, and H-R criteria, respectively. Furthermore, four sources were marked for at least RUWE and RV, three sources were marked for at least RV and H-R, 25 sources were marked for at least RUWE and H-R, and two sources were marked for all three criteria.

2.3. Estimating Effective Temperatures

We follow J. L. Curtis et al. (2020) in estimating the effective temperature T_{eff} of Blanco 1 by adopting a polynomial

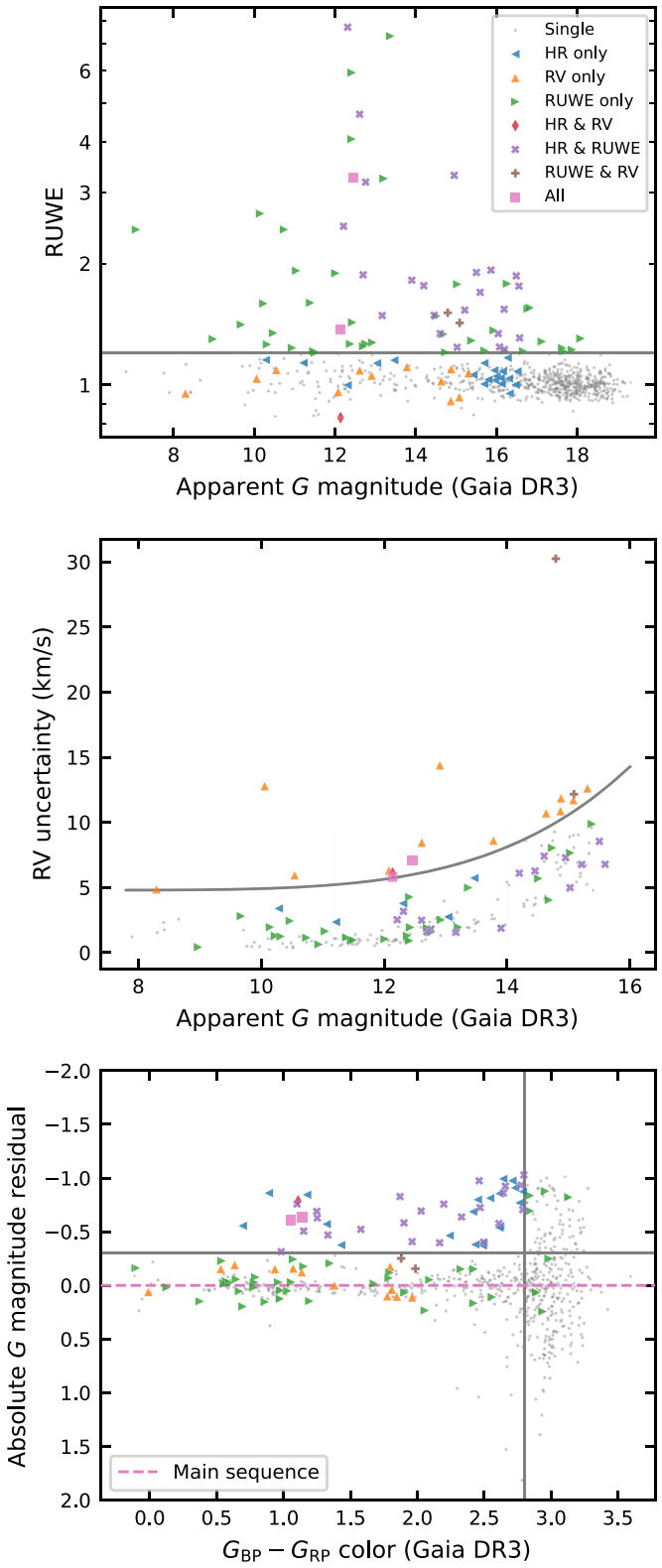

Figure 3. Gaia DR3 multiplicity indicators for Blanco 1 member candidates. Stars that are apparently single appear in gray. The acronyms in the legend are as follows. HR: on the binary sequence in the H-R diagram. RV: above the cutoff in RV uncertainty. RUWE: above the cutoff of the Gaia DR3 RUWE parameter.

that approximates conversion between dereddened Gaia DR2 $G_{BP} - G_{RP}$ color (D. W. Evans et al. 2018) and T_{eff}. This empirical color–T_{eff} relation is derived from benchmark stars reported by T. S. Boyajian et al. (2012), J. M. Brewer et al. (2016), and A. W. Mann et al. (2015) and the scatter implies a T_{eff} precision ≈ 50 K. To deredden the observed Gaia DR2 $G_{BP} - G_{RP}$ colors of our targets, we adopt $E(B-V) = 0.010$ from Gaia Collaboration et al. (2018a) as the color excess for Blanco 1, which we translate into Gaia DR2 $E(G_{BP} - G_{RP})$ color excess using the standard conversion $A_V = 3.1E(B-V)$ and the empirical relation $E(G_{BP} - G_{RP}) = 0.415A_V$ from J. L. Curtis et al. (2020). In carrying out these calculations, we used a Python implementation by L. G. Bouma et al. (2023). The resulting temperatures are listed in Table 1 for Blanco 1 candidates and are used to derive the temperature–rotation period relationship in Section 5.1.

2.4. Selecting a Comparison Sample of Field Stars

To assess whether the intrinsic rotation distribution of field stars might bias our interpretation of the candidate Blanco 1 members, we constructed a comparison sample of field stars for experimental control. Our selection procedure involved two steps. In the first step, we aimed to construct a set of field stars in the general vicinity of the Blanco 1 candidates. We began by selecting stars in the same HEALPix (K. M. Górski et al. 2005) level 4 pixels from the Gaia DR3 catalog, and then imposed the following limits in photometric magnitude, parallax, and proper motion:

1. Gaia G magnitude = 6.5–19.5,
2. parallax = 3.547–5.205 mas,
3. parallax relative error $< 10\%$, and
4. proper motion: exclude the following region around median cluster proper motion $(\mu_\alpha \cos\delta,\ \mu_\delta) \approx (18.71 \pm 2.5,\ 2.61 \pm 5)$ mas yr^{-1}.

The exclusion in proper motion space is important, as it helps eliminate unidentified members of Blanco 1 among the field stars (Figure 5). Applying these criteria resulted in 23,596 comparison sample candidates.

In the second step, we performed a one-to-one pairing between the Blanco 1 candidates and the comparison sample candidates. For each Blanco 1 candidate, we chose the most similar star within the same HEALPix level 4 pixel according to a similarity index that is the quadrature sum of the difference in Gaia G, G_{BP}, and G_{RP} magnitudes. If a star had already been matched to a previous Blanco 1 candidate, then we rejected it and moved on to the next most similar star. This procedure resulted in a matched sample of field stars that closely resemble Blanco 1 candidates in spatial, magnitude, and color distribution (Figures 4, 6). The selected field stars are listed in Table 2.

The effective temperatures of the comparison sample stars are derived using the same procedure as for the Blanco 1 stars in Section 2.3 and listed in Table 2. While the comparison stars are expected to be older than the benchmark stars used for the color–T_{eff} relation, our intention here is to calculate a temperature–rotation period relation as if the comparison stars are field stars contaminating the Blanco 1 candidates. Thus, even though the calculated T_{eff} may not accurately reflect the true T_{eff} of these likely older stars, they are sufficient for the purpose of establishing a comparison sample.

3. TESS Light Curves

The procedures described above yielded lists of 703 candidate Blanco 1 members and the same number of

Table 1
Columns for the Table of Blanco 1 Members

Column	Unit	Data type	Description
dr3_source_id	…	int64	Gaia DR3 source ID
dr2_source_id	…	int64	Gaia DR2 source ID
tic_id	…	int64	TESS Input Catalog (TIC) ID (TIC 8.2)
ra	deg	float64	Gaia DR3 R.A. (J2016.0)
ra_error	deg	float64	Gaia DR3 R.A. uncertainty (J2016.0)
dec	deg	float64	Gaia DR3 decl. (J2016.0)
dec_error	deg	float64	Gaia DR3 decl. uncertainty (J2016.0)
pmra	mas yr^{-1}	float64	Gaia DR3 proper motion in R.A. (J2016.0)
pmra_error	mas yr^{-1}	float64	Gaia DR3 proper motion uncertainty in R.A. (J2016.0)
pmdec	mas yr^{-1}	float64	Gaia DR3 proper motion in decl. (J2016.0)
pmdec_error	mas yr^{-1}	float64	Gaia DR3 proper motion uncertainty in decl. (J2016.0)
plx	mas	float64	Gaia DR3 parallax
plx_error	mas	float64	Gaia DR3 parallax uncertainty
phot_g_mean_mag	mag	float32	Gaia DR3 G magnitude
bp_rp	mag	float32	Gaia DR3 $G_{BP} - G_{RP}$ color
phot_g_abs_mag	mag	float32	Gaia DR3 absolute G magnitude, using distances from P21
ruwe	…	float32	Gaia DR3 RUWE
radial_veolicty	km s^{-1}	float32	Gaia DR3 RV
radial_veolicty_error	km s^{-1}	float32	Gaia DR3 RV uncertainty
teff	K	float32	Stellar effective temperature derived via the relation of J. L. Curtis et al. (2020; Section 2.3)
in_rt	…	bool	Flag for whether the target is within the tidal radius, using Galactic *XYZ* coordinates from P21
multi_ruwe_flag	…	bool	Flag for astrometric multiplicity as determined by Gaia DR3 RUWE
multi_rv_flag	…	bool	Flag for spectroscopic multiplicity as determined by Gaia DR3 RV uncertainty
multi_hr_flag	…	bool	Flag for photometric multiplicity as determined by Gaia DR3 color–magnitude diagram
has_cdips	…	bool	Whether the target has a valid CDIPS light curve
ls_period	day	float64	Rotation period determined by a Lomb–Scargle (LS) periodogram
ls_flags	…	string	Flags used in the vetting process (Section 4.1) for LS periods
gp_period	day	float64	Median rotation period of the Gaussian process (GP) model posterior
gp_perioderr1	day	float64	Upper uncertainty on the rotation period of the GP model posterior
gp_perioderr2	day	float64	Lower uncertainty on the rotation period of the GP model posterior

Note. The full table is available online in machine-readable format. The column descriptions are included here to demonstrate the table's content.
References. Gaia DR3: L. Lindegren et al. (2021). Gaia DR2: Gaia Collaboration et al. (2018b). TIC 8.2: K. G. Stassun et al. (2019) and M. Paegert et al. (2021). P21: X. Pang et al. (2021).

(This table is available in its entirety in machine-readable form in the online article.)

comparison field stars. To measure the photometric rotation periods of these two stellar samples, we used the full-frame images from the TESS primary mission (G. R. Ricker et al. 2015). All of the stars were observed in either Sectors 2 or 3 of the TESS primary mission, which spanned UT 2018 August 22–October 18. TESS observed full-frame images at a 30 minute cadence during its primary mission.

To make the light curves, we used the difference imaging pipeline (W. Bhatti et al. 2019) developed by the CDIPS project (L. Bouma 2019; L. G. Bouma et al. 2019). This pipeline performs forced-aperture photometry on difference images that are constructed on a sector-by-sector basis, by adding up the flux in circular apertures projected onto known stellar positions from Gaia DR2. The reference stellar fluxes in the TESS band are computed based on Gaia DR2. Since the default CDIPS target selection[5] did not include either the X. Pang et al. (2021) or the comparison field stars, we performed the photometry using difference images that were cached during the initial reductions of these fields. This procedure yielded 603 light curves for the cluster sample and 668 light curves for the comparison sample.[6] The remaining stars did not fall on the CCD sensors during the TESS primary mission. After considering the median point-to-point scatter of the light curves of the cluster members as a function of TESS magnitude, we adopted circular apertures with a radius of 1.5 pixels for stars brighter than a TESS magnitude of 13.3, and smaller 1 pixel radius circular apertures for fainter stars. This process yielded raw image-subtracted light curves (`IRM`), light curves corrected with a principal component analysis (`PCA`) cotrending approach described in Appendix B of L. G. Bouma et al. (2021), as well as measurements of any residual flux in a local annulus around each circular aperture (`BGV`). By default, we used the `PCA` time series when measuring rotation periods, but we used all three data sets to visually assess their validity, as described below.

4. Estimating Rotation Periods

4.1. Lomb–Scargle Periodograms

We adopted LS (N. R. Lomb 1976; J. D. Scargle 1982) periodograms as implemented by ASTROPY (Astropy Collaboration et al. 2013, 2018, 2022) as the main method for detecting rotation periods. For each sector's light curve of Blanco 1 candidates and comparison samples, we calculated LS periodograms over a frequency grid ranging from $1/27.4$ to 24 day^{-1}, with the lower limit corresponding to one sector of

[5] See the MAST documentation at https://archive.stsci.edu/hlsp/cdips.
[6] These light curves are available on Zenodo at DOI:10.5281/zenodo.10790463.

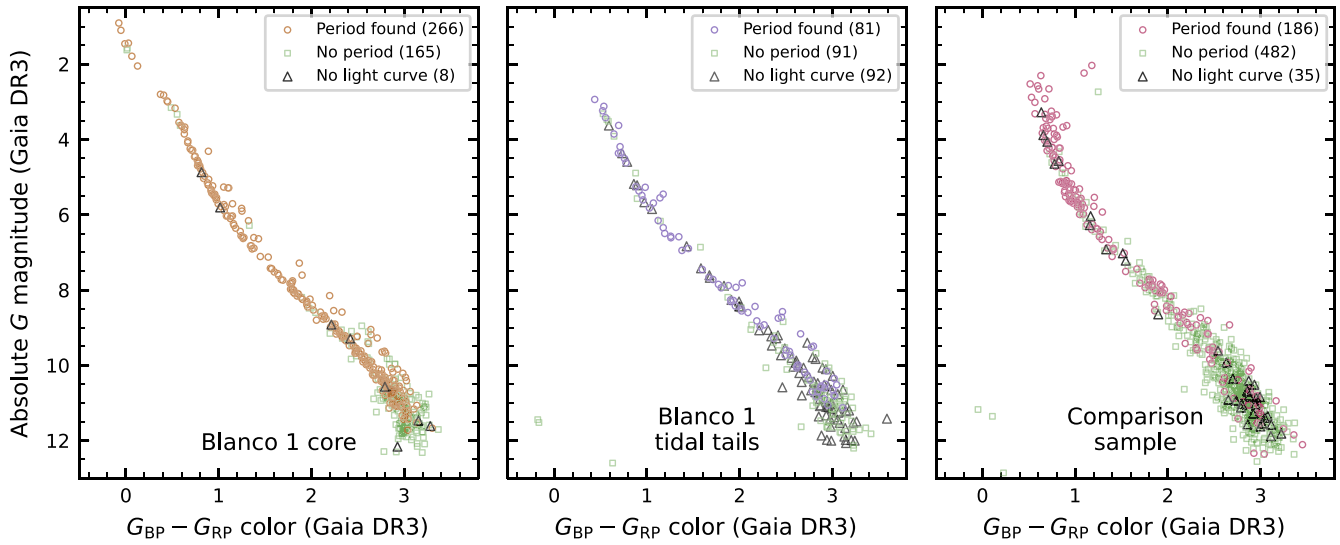

Figure 4. H-R diagrams of the open cluster Blanco 1 (left: core, center: tidal tails) and the comparison sample of field stars (right). Stars with measured rotation periods are plotted in circular marks of various colors, and those whose light curve shows no identifiable rotation signal are plotted in square purple marks. The gray triangular marks are the stars without valid light curves in the sample.

Table 2
Columns for the Table of Comparison Sample of Field Stars

Column	Unit	Data type	Description
dr3_source_id	…	int64	Gaia DR3 source ID
dr2_source_id	…	int64	Gaia DR2 source ID
tic_id	…	int64	TESS Input Catalog (TIC) ID (TIC 8.2)
match_dr3_source_id	…	int64	Gaia DR3 source ID of matched Blanco 1 member
ra	deg	float64	Gaia DR3 R.A. (J2016.0)
ra_error	deg	float64	Gaia DR3 R.A. uncertainty (J2016.0)
dec	deg	float64	Gaia DR3 decl. (J2016.0)
dec_error	deg	float64	Gaia DR3 decl. uncertainty (J2016.0)
pmra	mas yr $^{-1}$	float64	Gaia DR3 proper motion in R.A. (J2016.0)
pmra_error	mas yr $^{-1}$	float64	Gaia DR3 proper motion uncertainty in R.A. (J2016.0)
pmdec	mas yr $^{-1}$	float64	Gaia DR3 proper motion in decl. (J2016.0)
pmdec_error	mas yr $^{-1}$	float64	Gaia DR3 proper motion uncertainty in decl. (J2016.0)
phot_g_mean_mag	mag	float32	Gaia DR3 G magnitude
bp_rp	mag	float32	Gaia DR3 $G_{BP} - G_{RP}$ color
phot_g_abs_mag	mag	float32	Gaia DR3 absolute G magnitude, using Gaia DR3 parallax
teff	K	float32	Stellar effective temperature derived via the relation of J. L. Curtis et al. (2020; Section 2.3)
has_cdips	…	bool	Whether the target has a valid CDIPS light curve
ls_period	day	float64	Rotation period determined by an LS periodogram
ls_flags	…	string	Flags used in the vetting process (Section 4.1) for LS periods

Note. The full table is available online in machine-readable format. The column descriptions are included here to demonstrate the table's content.
References. Gaia DR3: L. Lindegren et al. (2021). Gaia DR2: Gaia Collaboration et al. (2018b). TIC 8.2: K. G. Stassun et al. (2019) and M. Paegert et al. (2021).
(This table is available in its entirety in machine-readable form in the online article.)

TESS observations and the upper limit the Nyquist frequency of the 30 minute cadence. The grid spacing was chosen adaptively by ASTROPY to have roughly five grid points per significant periodogram peak. We also generated an LS periodogram for the window function, which takes a value of unity for each observed sample. For each sampled periodogram, we recorded the five highest local maxima as the five most significant peaks, and calculated their false-alarm probability with the bootstrap method (Ž. Ivezic et al. 2014; J. T. VanderPlas 2018).

We then manually vetted the detected periodogram peaks in order to identify the most likely true period and to eliminate insignificant peaks (false-alarm probability of 4σ). For reference during the vetting process, we also generated phase-folded light curves (PCA time series) at the five most significant periodogram peaks, as well as the unfolded PCA, IRM, and BGV time series, in order to identify light curves suffering from instrumental or systematic anomalies and exclude them from the detected periods. Among stars with a valid CDIPS light curve, we detected likely rotation periods for 47% of the candidate tidal tail members and 62% of the core members, while the comparison sample of field stars yielded rotation period detection for only 28%. As Figure 4 shows, we detected rotation periods in a fewer proportion of stars toward the cooler end of the H-R diagram. Since these stars are dimmer in apparent and absolute brightness, it is likely that the

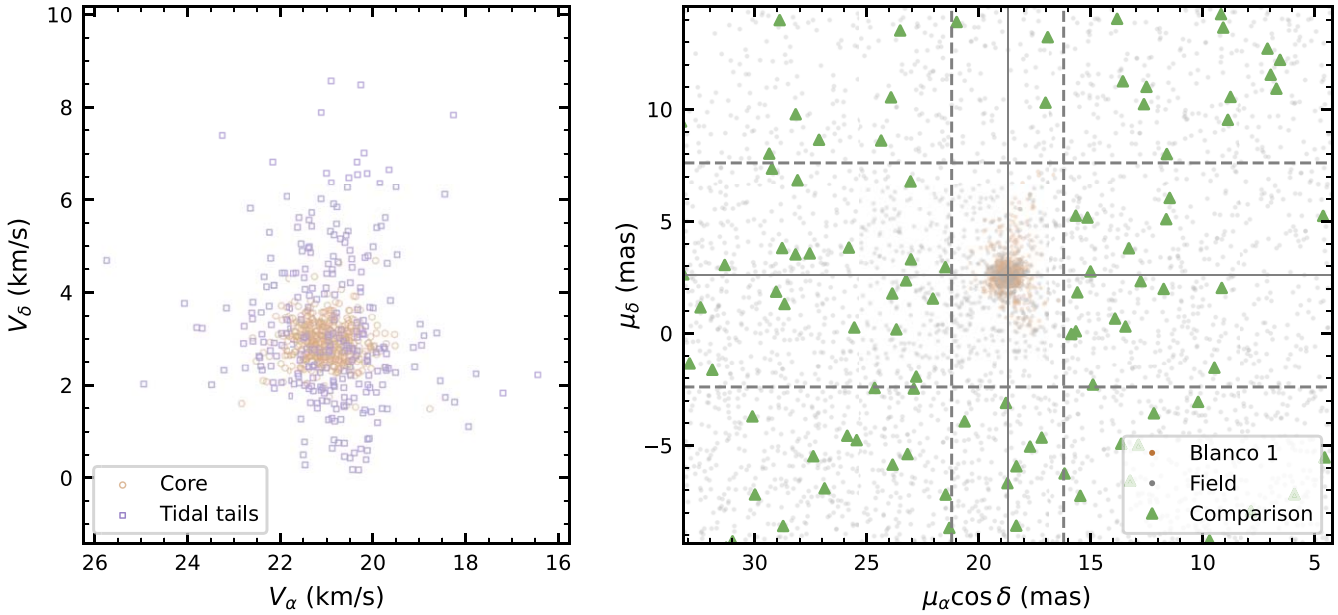

Figure 5. Left: proper motion of Blanco 1 member candidates, converted into physical units using the corrected distances by X. Pang et al. (2021). The circular orange marks are the stars in the cluster core, and the square magenta marks are those in the tidal tails. Right: exclusion in proper motion space for the comparison sample. The orange marks are Blanco 1 candidates, and the gray marks are field stars satisfying the first three criteria outlined in Section 2.4 (i.e., before the exclusion in proper motion space). The triangular purple marks are stars in the selected comparison sample. A box of ± 2.5 mas yr^{-1} in μ_α and ± 5 mas yr^{-1} in μ_δ (shown in dashed gray lines) centered at $(\mu_\alpha, \mu_\delta) \approx (18.71, 2.61)$ mas (indicated by solid thin gray lines) is drawn to exclude potentially unidentified members of the Blanco 1 cluster from contaminating the sample.

amplitudes of their rotation signals, if present, fall below the detection threshold of TESS.

Flags used in manual vetting. In the vetting process, we made use of several flags as summarized in Table 3. Detailed descriptions of the flags are as follows.

1. *A*. The periodogram contains multiple peaks that correspond to plausible phase-folded light curves. These peaks are often the true period and its first harmonic (period ratio of 2:1), but can also be multiple peaks for stars showing complicated oscillations.
2. *B*. The sources either show variations that resemble those of eclipsing binaries, or there are nearby sources in the target list that show variations at roughly the same period, indicating a possible blend.
3. *D*. The detrended time series (`PCA`) shows artifacts that are not present in the original (`IRM`) time series.
4. *F*. The light curve shows a flare-like systematic, where the magnitude increases sharply by more than 0.5 mag and then drops down to the original magnitude within 1 day.
5. *G*. The original or detrended time series shows correlation with the background flux values (`BGV` column in the FITS file). In this case, the first peak that does not correspond to variations in `BGV` (i.e., due to end-of-orbit scattered light) is selected. If all detected periodogram peaks can be entirely explained by this correlation, then the source is marked as no valid period detected.
6. *M*. The detected rotational signal is marginal. The amplitude is comparable to the scatter.
7. *I*. The light curve is affected by instrumental effects, such as scattered light.
8. *V*. The light curve shows stellar activity or variability that deviates from a regular sinusoid.

These flags are reported in Tables 1 and 2. We found, however, that excluding targets from later analysis based on the flags here do not significantly alter the resulting the temperature–rotation period distribution (Section 5.1), so we report these flags here largely in the interest of transparency and in the hope that it will be useful to future studies of Blanco 1.

4.2. Gaussian Process Regression

We used a GP to model quasiperiodic covariance in the light-curve time series. In constructing the GP model and sampling the posterior distribution of its parameters, we aim to estimate the uncertainty of the detected rotation period in the light curves. Further motivation for adapting GP regression to measure stellar rotation periods is described in the previous rotation period study of Blanco 1 by E. Gillen et al. (2020), which built on the work by R. Angus et al. (2018). Here, we broadly follow the method of E. Gillen et al. (2020) and adopted `RotationTerm` from the Python package CELERITE2 (D. Foreman-Mackey et al. 2017; D. Foreman-Mackey 2018) as our GP kernel, and we include its full definition in this section for the sake of completeness. Unlike E. Gillen et al. (2020), however, we omit their nonperiodic term in the GP kernel since our chosen light-curve time series (`PCA`; see Section 3) has already been detrended.

The `RotationTerm` kernel is a mixture of two simple harmonic oscillator (SHO) terms, each with a power spectrum density (PSD)

$$\mathcal{S}[S_0, Q, \omega_0](\omega) = \sqrt{\frac{2}{\pi}} \frac{S_0\, \omega_0^4}{(\omega^2 - \omega_0^2)^2 + \omega_0^2 \omega^2 / Q^2}, \quad (3)$$

where ω is the angular frequency argument of the PSD and the amplitude S_0, quality factor Q, and resonant frequency ω_0 are parameters of the GP term (E. R. Anderson et al. 1990;

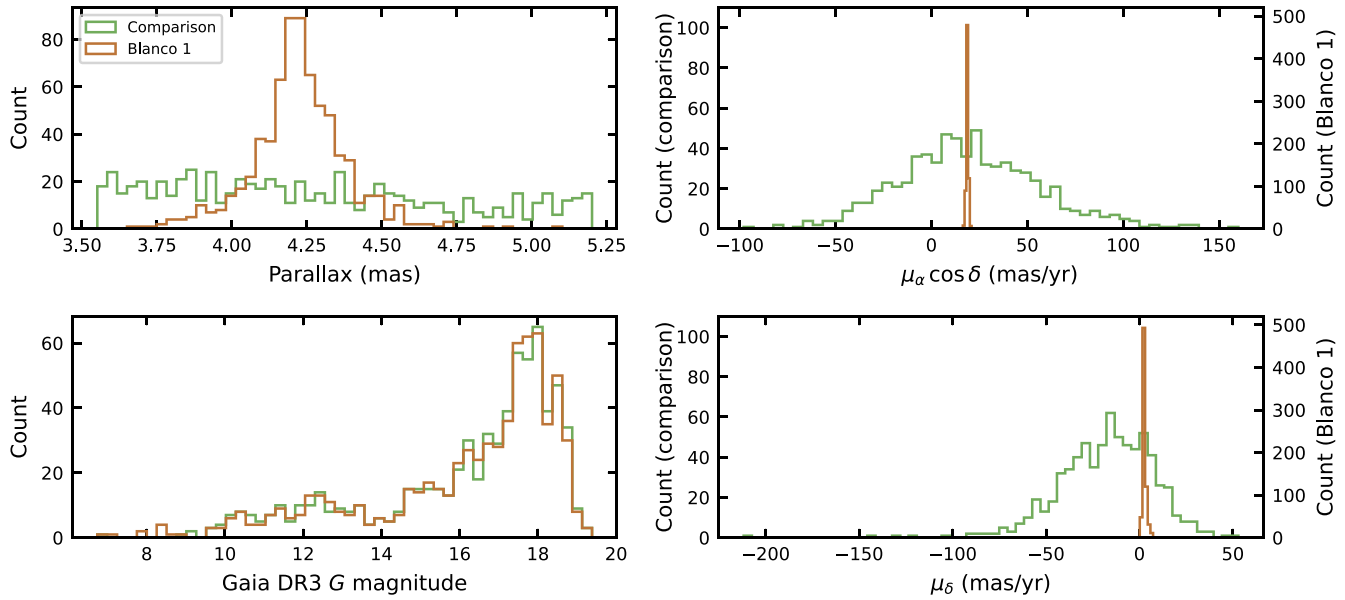

Figure 6. Histograms comparing the Blanco 1 member candidates (orange lines) and the selected comparison sample of field stars (purple lines). Top left: parallax histograms. The Blanco 1 candidates shows a clustering in parallax, while the comparison sample is evenly distributed. Top and bottom right: proper motion histograms. The Blanco 1 candidates show a sharp peak in proper motion space, and they are plotted on a different scale (right y-axis) for convenience. The comparison sample excludes those peaks; see also Figure 5. Bottom left: Gaia DR3 G-magnitude histograms. The distributions for Blanco 1 candidates, and the comparison sample closely match.

Table 3
Flags Used in the Vetting Process for Lomb–Scargle Periods

Flag	Description
A	Period aliases present/ambiguous period
B	Possible blend or eclipsing binary
D	Detrending (PCA) artifacts
F	Possible spikes or flares
G	Background (BGV) correlation
I	Affected by instrumental effects/scattered light
M	Marginal amplitude
V	Variable star/stellar activity

D. Foreman-Mackey et al. 2017). The two SHO terms are at the fundamental period P and first harmonic (half) period $P/2$. For the ease of interpretation, these parameters are expressed in terms of a standard-deviation-like parameter σ, base quality factor Q_0, difference in quality factor between the fundamental and first harmonic δQ, and fractional power of the first harmonic f, such that for the PSD of the two SHO terms $\mathcal{S}[S_1, Q_1, \omega_1]$ and $\mathcal{S}[S_2, Q_2, \omega_2]$

$$A = \frac{\sigma^2}{1+f}, \tag{4a}$$

$$S_1 = \frac{A}{\omega_1 Q_1}, \qquad S_2 = \frac{fA}{\omega_2 Q_2}, \tag{4b}$$

$$Q_1 = Q_2 + \delta Q, \qquad Q_2 = \frac{1}{2} + Q_0, \tag{4c}$$

$$\omega_1 = \frac{4\pi Q_1}{P\sqrt{4Q_1^2 - 1}}, \qquad \omega_2 = 2\omega_1. \tag{4d}$$

This parameterization has the advantage that if $Q_0 > 0$ and $\delta Q > 0$, then the GP is guaranteed to be underdamped and the fundamental term has higher quality than the first harmonic. Because the GP is otherwise centered on 0, it is offset by a mean term μ.

We used PyMC (J. Salvatier et al. 2015; O. Abril-Pla et al. 2023) to sample the posterior of the GP parameters. PyMC uses the No-U-Turn Sampler (M. D. Hoffman & A. Gelman 2014) to perform Hamiltonian Monte Carlo sampling (S. Duane et al. 1987). We set the prior distributions for the `RotationTerm` parameters as

$$\ln(P/d) \sim \mathcal{N}(\ln(P_{\rm LS}/d), 0.2), \tag{5a}$$

$$\ln\sigma \sim \mathcal{N}(\text{standard deviation of magnitude}, 2), \tag{5b}$$

$$\ln Q_0 \sim \mathcal{U}(-50, 50), \tag{5c}$$

$$\ln \delta Q \sim \mathcal{U}(-50, 50), \tag{5d}$$

$$f \sim \mathcal{U}(0, 1), \tag{5e}$$

$$\mu \sim \mathcal{N}(\text{median magnitude}, 1), \tag{5f}$$

where $\mathcal{U}(a, b)$ is the uniform distribution on the interval (a, b) and $\mathcal{N}(m, s)$ is a normal distribution with mean m and standard deviation s. The median posterior value and the 1σ uncertainty corresponding to the 68% highest density interval of the GP period is listed in Table 1 for Blanco 1 candidates.

5. Verifying Blanco 1's Tidal Tails with Gyrochronology

5.1. Temperature–Rotation Period Distribution

The Blanco 1 candidates ranging from mid-F to mid-K dwarfs (4400 K $\leqslant T_{\rm eff} <$ 6200 K) show a well-defined temperature–rotation period, or gyrochrone, sequence. Figure 7 compares the temperature–period relation of single-star Blanco 1 candidates in Figure 7, to members of the similarly aged Pleiades cluster and the older Praesepe cluster. In constructing Figure 7, we estimated stellar effective temperatures from Gaia DR2 $G_{\rm BP} - G_{\rm RP}$ color using the method described in Section 2.3 for all three clusters, and we use the rotation period measurements from

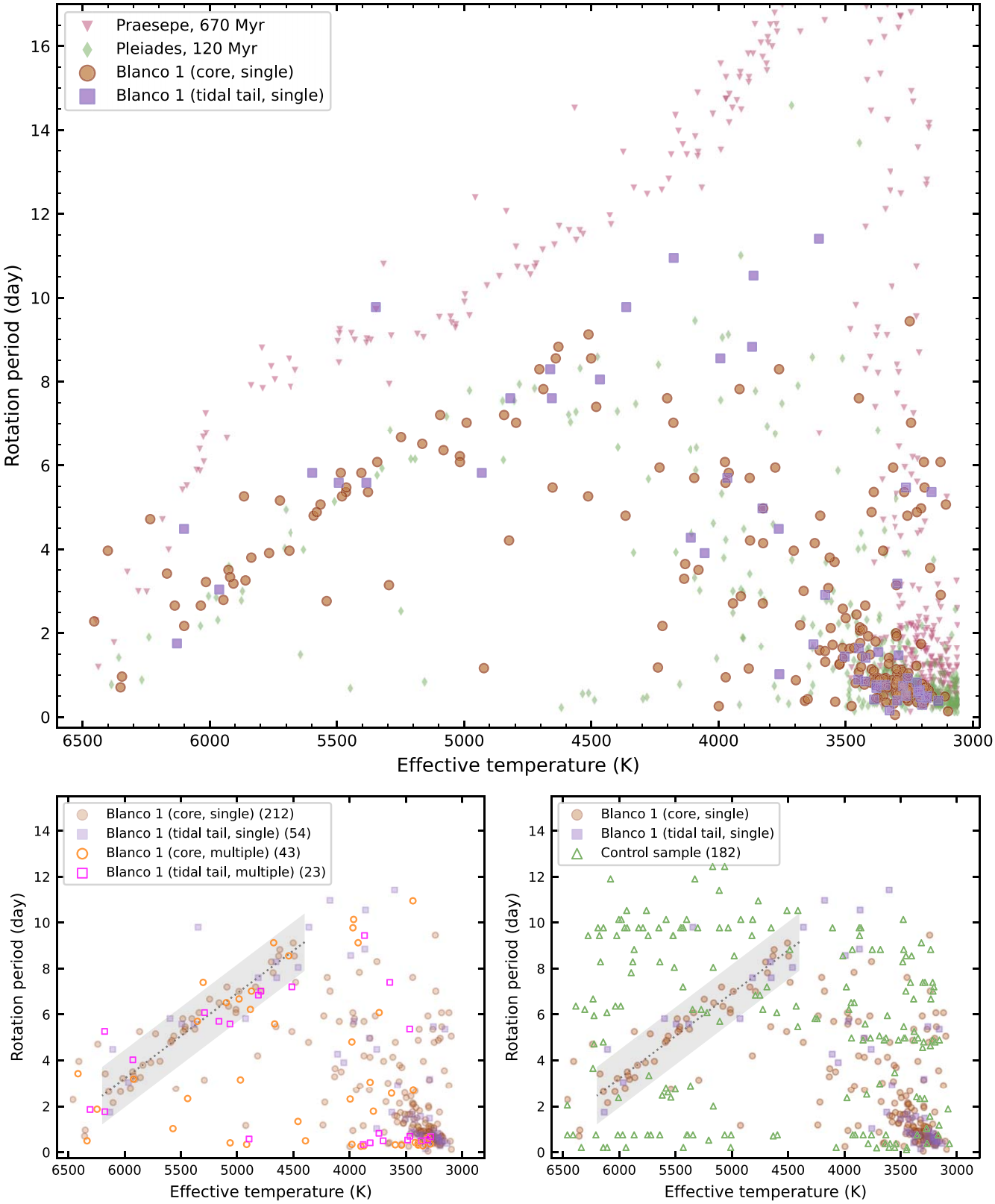

Figure 7. Temperature–rotation period diagrams. Top: apparently single stars in Blanco 1 and benchmark comparison clusters. Bottom left: single and multiple stars in Blanco 1. Bottom right: Blanco 1 and comparison sample stars. For Blanco 1, the circular marks are core stars that fall within the tidal radius estimated by X. Pang et al. (2021), and the square marks are those that are outside the tidal radius, i.e., in the tidal tails. The effective temperatures are derived from Gaia DR2 $G_{\rm BP} - G_{\rm RP}$ colors using an empirical relation derived by J. L. Curtis et al. (2020). The gray dashed lines in the bottom panels indicate the gyrochrone of Blanco 1, with the shaded region being the $\pm$1.25 day band where we consider a star to fall within the gyrochrone.

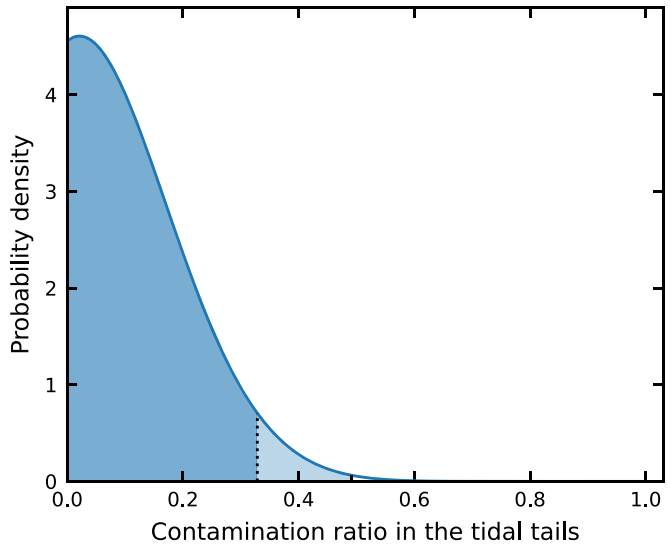

Figure 8. Posterior distribution for the contamination ratio of the tidal tail candidates in Blanco 1. The shaded regions indicate the 2σ and 3σ intervals starting from zero, with the respective upper limits highlighted in black lines.

L. M. Rebull et al. (2016) for the Pleiades and R. Rampalli et al. (2021) for Praesepe.

As expected, Blanco 1's gyrochrone sequence, which we visualize as the shaded band around the gray dashed line in the bottom panels of Figure 7), broadly overlaps the Pleiades and lies far below Praesepe, consistent with previous findings by P. A. Cargile et al. (2014) and E. Gillen et al. (2020). The M dwarfs, on the other hand, show a large scatter in their rotation periods, consistent with many of them not having converged onto the zero-age main sequence. There is a single outlier, Gaia DR3 2333895128547040768, among the FGK stars ($T_{\rm eff} \approx 5300$ K) in the tidal tails that has a rotation period (9.77 days) clearly too long to be part of the gyrochrone. After cross-checking its light curves in later TESS Sectors 29 and 69, we determined that the detected period is likely double the true period of ≈5 days. This high degree of conformance to the gyrochrone indicates that the tidal tail candidates from X. Pang et al. (2021) likely have a low rate of contamination rate from unrelated field stars. We formally compute the posterior distribution of this contamination rate in Section 5.2.

5.2. Contamination in the Tidal Tails

We estimate the contamination rate of the tail stars by comparing how many stars in the core and tail conform to the gyrochrone. In determining the gyrochrone, we restrict to targets from 4400 to 6200 K, which excludes M dwarfs and lower-mass K dwarfs as well as stars with temperatures above the Kraft break. Then, we iteratively fit a line to the gyrochrone using Blanco 1 stars by rejecting stars that fall more than 1.25 days from the fitted line at each step. Once the line fitting converges, we count the fraction of stars falling within 1.25 days of the gyrochrone for the cores stars ($g_{\rm core}$) and the comparison sample ($g_{\rm comp}$). Assuming that all core stars are true members and that the comparison sample may have a certain fraction of Blanco 1 stars, we can calculate the probability p that a star in the tidal tail is within the gyrochrone range

$$p = (1 - c)g_{\rm core} + cg_{\rm comp} = c(g_{\rm comp} - g_{\rm core}) + g_{\rm core}, \quad (6)$$

given a contamination ratio c for the tidal tails. The probability that k out of n tidal tail stars fall within the gyrochrone given this probability p is given by the binomial distribution

$$\Pr(k; n, p) = \binom{n}{k} p^k (1 - p)^{n-k}. \quad (7)$$

Assuming a flat prior for the contamination ratio $c \in [0, 1]$, we can marginalize this probability distribution over c to obtain its posterior distribution

$$\Pr(c; n, k) = \mathcal{C}^{-1} p^k (1 - p)^{n-k}, \quad (8)$$

where $\mathcal{C}$ is a normalization factor given by the unsigned definite integral

$$\mathcal{C} = \left| \int_0^1 p^k (1 - p)^{n-k}\, dc \right| = \int_{g_{\rm comp}}^{g_{\rm core}} p^k (1 - p)^{n-k}\, dp. \quad (9)$$

Thus, we arrive at the posterior distribution for the contamination of the tidal tails.

Using the formalism established in the previous paragraph, we measure gyrochrone fractions $g_{\rm core} = 0.741$ for the core stars and $g_{\rm comp} = 0.0847$ for the comparison sample. There are $k = 16$ out of $n = 22$ tidal tail stars in the range of 4400 K $\leqslant T_{\rm eff} <$ 6200 K that are in the gyrochrone. Plugging these values into Equation (8) yields the posterior distribution

$$\Pr(c) = \mathcal{C}^{-1}(0.741 - 0.656c)^{16}(0.259 + 0.656c)^6, \quad (10)$$

where $\mathcal{C}^{-1} \approx 1.828 \times 10^6$. As visualized in Figure 8, the posterior is consistent with zero contamination, and the 2σ and 3σ upper limits on the contamination ratio are 0.33 and 0.49, respectively.

6. Discussion

6.1. Confirmation of Blanco 1's Tidal Tails

Our rotation period measurements serve to independently confirm that the recently discovered tidal tails are truly associated with the young open cluster Blanco 1. Previous work (Y. Li et al. 2021; S. Meingast et al. 2021; X. Pang et al. 2021) identified this extended structure based on Gaia DR2 and DR3 spatio-kinematic data alone. By checking that these new cluster member candidates conform to the expected gyrochrone sequence of the core cluster members, we have ruled out with high statistical confidence that they can be explained by contamination from field stars (Section 5.2). In fact, the contamination is low enough (<0.33 at 2σ) to enable further studies, such as morphology, dynamics, and planetary occurrence rate, of Blanco 1.

Now that we have confirmed the validity of its tidal tails, we can revisit and confirm previous authors' conclusions on the structure of Blanco 1 in the Galaxy. Adopting the values of X. Pang et al. (2021), Blanco 1 is located almost directly below the Galactic plane (Figure 9), at a distance of approximately 240 pc from the Sun. It has a tight core of ≈300 stars, within a tidal radius of 10.2 pc (Figure 10). The spatial distribution of the core stars is elongated in the direction almost perpendicular (inclined by ≈78°) to the Galactic plane (Figure 9),[7] which X. Pang et al. (2021) hypothesized may be due to core stars evaporating via

[7] The line of sight to Blanco 1 is also almost perpendicular to the Galactic plane, raising the question of whether this elongation is an artifact of inverting the parallax. It turns out that X. Pang et al. (2021) already corrected for this effect through a Bayesian framework. Tellingly, for the Coma Berenices cluster, which is located near the Galactic north pole, X. Pang et al. (2021) did not find such an elongation perpendicular to the Galactic plane, which indicates that this elongation of the Blanco 1 core is likely real.

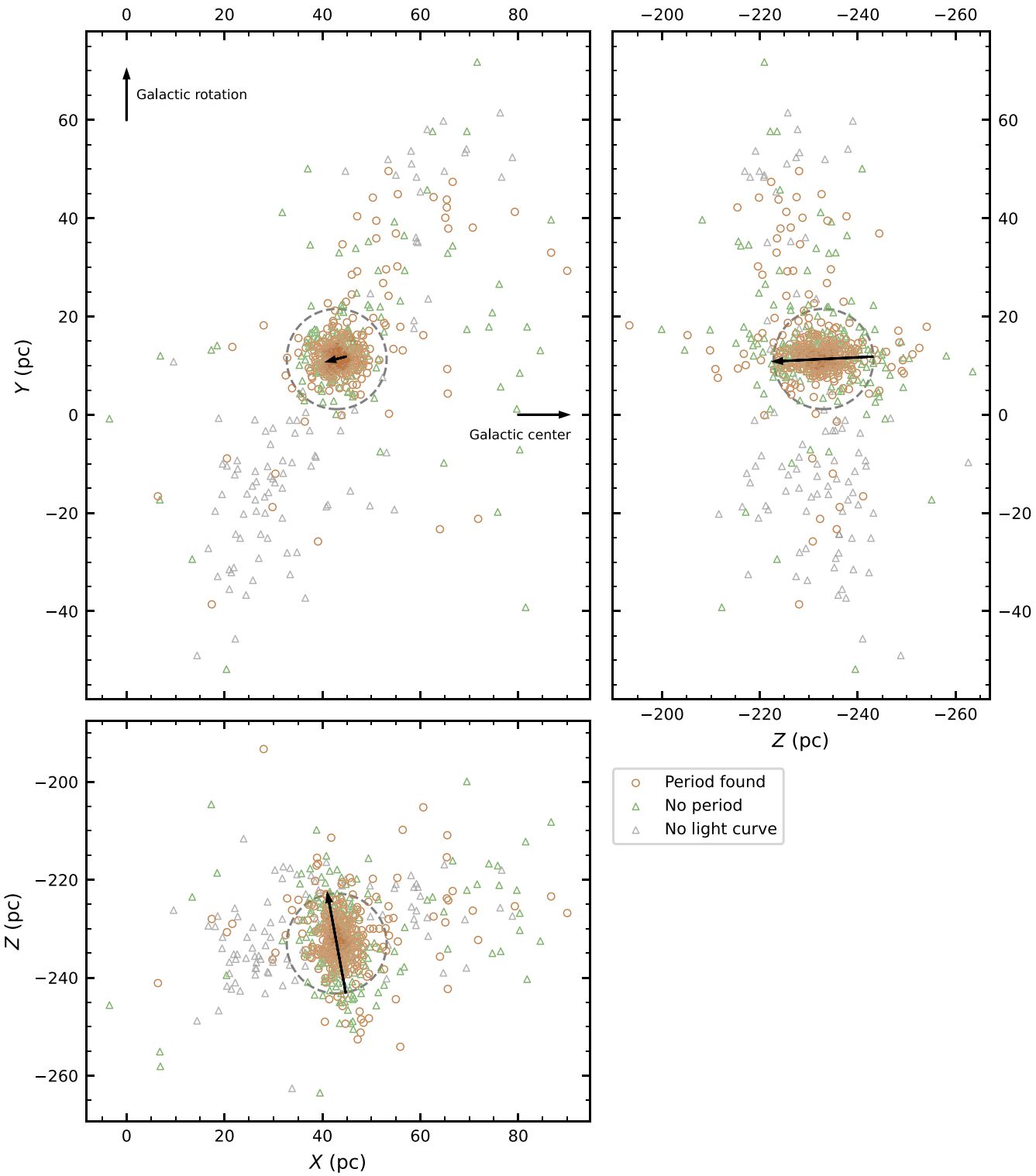

Figure 9. Blanco 1 members in Galactic Cartesian coordinates *XYZ*, as determined by X. Pang et al. (2021). The dashed gray circle indicates the nominal tidal radius determined by X. Pang et al. (2021), and the black arrow within the circle is the projected direction to the Sun. The circular orange marks are the stars with an actually measured rotation period, and the triangular gray marks are those without a measured period.

the L1 and L2 Lagrange points in the Galactic tidal field, similar to the *N*-body simulation results by A. H. W. Kupper et al. (2008).

The reported extent of the cluster, however, is much larger. Despite being unbound and much less dense, the stars outside of the tidal radius contain ≈37% of the mass of the cluster (Y. Li et al. 2021). They protrude in opposite directions from the cluster core, each extending 50–60 pc from the cluster center. The leading and trailing tails are slightly misaligned with the direction of cluster rotation about the Galactic center, consistent with them being the result of differential rotation (S. Meingast et al. 2021).

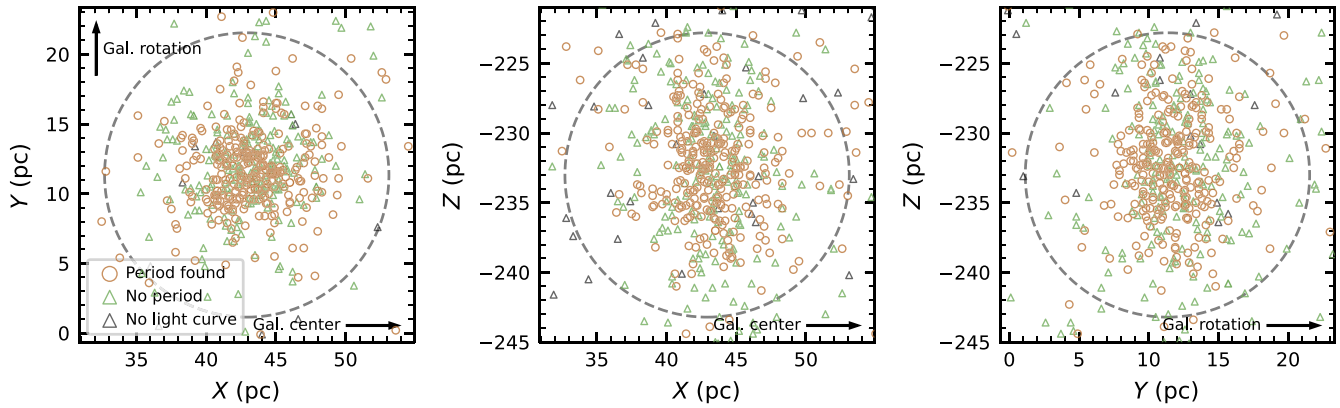

Figure 10. Blanco 1 core members in Galactic Cartesian coordinates *XYZ*, as determined by X. Pang et al. (2021). The dashed gray circle indicates the nominal tidal radius determined by X. Pang et al. (2021). The circular orange marks are the stars with a measured rotation period, and the triangular gray marks are those without a measured period.

6.2. How Complete is the Local Young Star Census?

Having confirmed Blanco 1's tidal tails using TESS photometric rotation periods, we would like to know to what extent this strategy can be extended to other nearby young open clusters. Answering this question would give us an idea of how complete our current local young star census is and thereby allow us to assess the future impact of these tidal tail stars on the search for young exoplanets. To this end, we will make a back-of-the-envelope estimation of what fraction the presently identified sample of tidal tail stars is in terms of all nearby young stars where TESS is sensitive to detecting transiting planets.

We begin by considering how many stars have been identified in the literature as candidates for the tidal tails of nearby young open clusters. Querying the Montreal Open Clusters and Associations (MOCA) database (J. Gagné et al. 2024, in preparation; J. Gagné et al. 2018; J. Gagné 2024), there are 32 open clusters younger than 300 Myr within 300 pc. The MOCA database reports that 13 of these open clusters have detected tidal tails ("coronae") in the literature. Furthermore, the MOCA database reports that the core of these open clusters contain ≈10,000 likely candidate members, while their tidal tails contain ≈4600 likely candidates. Using Gaia $G_{\rm RP} < 13$ as a rough limit of TESS planet detection narrows them down to ≈2800 core versus ≈1100 tidal tail candidates.

We then consider the number of all nearby young stars that are within TESS's planet detection limit. A quick query of the Gaia DR3 catalog yields $\approx 7.2 \times 10^6$ sources with good parallax measurements ($\varpi/\sigma_\varpi > 10$) within 300 pc, $\approx 1.4 \times 10^6$ of which have $G_{\rm RP} < 13$. Using a uniform age distribution of 0–10 Gyr as a zeroth-order approximation, we arrive at $\approx 4.1 \times 10^4$ stars younger than 300 Myr within this volume whose transiting planets TESS is potentially sensitive to. This implies that the presently known core and tidal tail candidates respectively constitute ≈11% and ≈3% of stars within 300 pc younger than 300 Myr whose potentially transiting planets TESS may be sensitive to.

6.3. Searching for Young Exoplanets in Tidal Tails

Even though open cluster candidates are a relatively small fraction of young nearby stars, they have the advantage that their age is easily determined compared to field stars. However, to date, we know relatively few planets in open clusters. Predating TESS and Gaia DR2, J. L. Curtis et al. (2018) listed <30 planets discovered in clusters, most of which were discovered by Kepler and K2. More recently, Y.-Z. Dai et al. (2023) compiled a list of 73 confirmed planets and 84 planet candidates crossmatched to the $\sim 10^6$ stars in ≈8000 groups identified by M. Kounkel et al. (2020) out to 3 kpc. Considering that not all of these ≈8000 groups are necessarily "open clusters" in the traditional sense, this list of ∼100 confirmed and candidate planets is a drop in the bucket compared to the ≈4000 likely candidate members of nearby young open clusters amenable to transit detection by TESS. Regardless of whether this dearth is the result of detection efficiency or intrinsic rarity, expanding the number of target stars in well-dated open clusters will be crucial to the search for more young planets.

In particular, tidal tail candidates can have an outsize impact in turning previously assumed field stars with poor age constraints into open cluster members with tight age constraints. If we assume an average tidal dissolution timescale of ≈100 Myr for open clusters, then it becomes even more important to identify the dissolved cluster remnants with low spatial density as cluster age increases. As an extreme example, T. Jerabkova et al. (2021) identified over 800 tidal tail candidates of the Hyades open cluster spanning a spatial extent of 800 pc.

The identification and confirmation of tidal tail candidates can thus have a real impact on age determination for nearby young stars, and, by extension, young exoplanets. As T. Jerabkova et al. (2021) pointed out, independent methods of verification such as rotation periods are crucial in verifying candidates in a diffuse structure based on spatio-kinematic data alone, since the membership probability from clustering algorithms is not sufficiently reliable. If Blanco 1 can be used as a guide, we may double the number of targets for planet searches by including tidal tail candidates in addition to the core candidates. Our calculation in Section 5.2 suggests that the contamination rate of these tidal tail candidates is probably low enough to enable occurrence rate studies of these young planets.

Thanks to its unique mission design, TESS is well positioned to contribute to the search for young planets in the tidal tails of nearby young open clusters by both improving the local young star census and the transit observation coverage. This paper demonstrates that TESS can improve the local young star census by verifying spatio-kinematic membership through stellar rotation period measurements. Since young stars <1 Gyr are

not expected to have rotation periods much longer than one TESS spacecraft orbit of 13.7 days, the limited observational baseline of TESS sectors in its prime mission and first two extended missions becomes irrelevant. Thus, TESS's all-sky coverage opens up all nearby open clusters for similar rotation period studies. If we narrow our focus further to the relatively diffuse tidal tails, we may entirely overstep the problem of crowding in TESS's relatively big (21″) pixels for transit searches. In summary, there remains deep potential for TESS to find yet more young planets in its continuing service.

7. Conclusion

In this study, we have used light curves derived from TESS full-frame images to measure the rotation periods of member candidates in the young open cluster Blanco 1 and comparison field stars and derived stellar effective temperature–rotation period diagrams for them. Based on the gyrochrone sequence identified in the temperature–period diagrams, we conclude that stars in the proposed tidal tails of Blanco 1 and those in the core of the cluster are broadly consistent in age, with few outliers. We detected rotation periods within 1.25 days of the gyrochrone for 72% of the candidate tidal tail members and 74% of the core members within a stellar effective temperature range of 4400–6200 K, while a comparison sample of field stars yielded analogous rotation period detection for only 8.5%. Given these detection rates, we find the contamination ratio for the tidal tails is consistent with zero and <0.33 at the 2σ level, confirming the existence of the tidal tails. The relatively low contamination also suggests that finding more tidal tails of known clusters and associations is a viable strategy for mapping out the dissolution of nearby open clusters through a more complete local young star census. Ultimately, this strategy could broaden the search for new exoplanets in nearby young star clusters and associations, leading to a determination of their occurrence rate.

Acknowledgments

The corresponding author would like to thank Michael V. Maseda, in whose class this paper originated as a project.

This paper includes data collected by the TESS mission that are publicly available from the Mikulski Archive for Space Telescopes (MAST) in the CDIPS High Level Science Product (L. Bouma 2019) at doi:10.17909/t9-ayd0-k727. We acknowledge the use of public TESS data from pipelines at the TESS Science Processing Operations Center (SPOC). Resources supporting this work were provided by the NASA High-End Computing (HEC) Program through the NASA Advanced Supercomputing (NAS) Division at Ames Research Center for the production of the SPOC data products. Funding for the TESS mission is provided by NASA's Science Mission Directorate.

This work has made use of data from the European Space Agency (ESA) mission Gaia, processed by the Gaia Data Processing and Analysis Consortium (DPAC). Funding for the DPAC has been provided by national institutions, in particular the institutions participating in the Gaia Multilateral Agreement. This research made use of the Montreal Open Clusters and Associations (MOCA) database, operated at the Montréal Planétarium (J. Gagné et al. 2024, in preparation).

Facilities: Gaia and TESS.

Software: Astropy (Astropy Collaboration et al. 2013, 2018, 2022), Astroquery (A. Ginsburg et al. 2019), Celerite2 (D. Foreman-Mackey et al. 2017; D. Foreman-Mackey 2018), CDIPS pipeline (W. Bhatti et al. 2019), ligo.skymap, Matplotlib (J. D. Hunter 2007; Matplotlib Development Team 2023), Numpy (C. R. Harris et al. 2020), Pandas (W. McKinney 2010; Pandas Development Team 2023), PyMC, and Scipy (P. Virtanen et al. 2020).

Appendix A
Crossmatching Candidates of Blanco 1 Members

In producing Figure 1, we crossmatched lists of candidate Blanco 1 members by eight authors: Gaia Collaboration et al. (2018a), T. Cantat-Gaudin et al. (2018), Y. Zhang et al. (2020), S. Meingast et al. (2021), X. Pang et al. (2021), Y. Tarricq et al. (2022), Z. He et al. (2022), and J. Alfonso & A. García-Varela (2023). The result of the crossmatch is Table A1, with distinct candidates indexed by their Gaia DR3 and DR2 source IDs and Boolean flags indicating whether a candidate is present a given reference. As Y. Zhang et al. (2020) did not include Gaia source IDs in their table, we included a column that gives their table's row index if a candidate is present there.

In the final stages of preparing this paper, we became aware of the work by E. L. Hunt & S. Reffert (2023), which contains a membership list for Blanco 1 as part of their comprehensive all-sky catalog of open clusters. Although their list has more members ($N = 841$) than X. Pang et al. (2021) ($N = 703$), we still prefer the latter's for the analysis in this paper as they provide corrected distances and the conversion to Galactic Cartesian coordinates.

Table A1
Columns for the Table of Blanco 1 Candidates in Literature References

Column	Data Type	Description
dr3_source_id	int64	Gaia DR3 Source ID
dr2_source_id	int64	Gaia DR2 Source ID
zhang_num	int16	Index column in Table 1 of Y. Zhang et al. (2020)
alfonso_flag	bool	Flag for J. Alfonso & A. García-Varela (2023)
he_flag	bool	Flag for Z. He et al. (2022)
tarricq_flag	bool	Flag for Y. Tarricq et al. (2022)
pang_flag	bool	Flag for X. Pang et al. (2021)
meingast_flag	bool	Flag for S. Meingast et al. 2021
zhang_flag	bool	Flag for Y. Zhang et al. (2020)
cantat_gaudin_flag	bool	Flag for T. Cantat-Gaudin et al. 2018
gaia_collab_flag	bool	Flag for Gaia Collaboration et al. 2018a

Note. Only the columns of this table are shown here to demonstrate its form and content. A machine-readable version of the full table is available online. The flag columns indicate whether a source is listed as a candidate member of Blanco 1 in the provided reference.

(This table is available in its entirety in machine-readable form in the online article.)

Appendix B
Main Sequence of Blanco 1

Table B1 gives the coefficients for an empirical polynomial fit to the main sequence of Blanco 1 in Gaia DR3 $G_{BP} - G_{RP}$ colors and G magnitudes, adopting the Blanco 1 candidates of X. Pang et al. (2021). These magnitudes are converted to the absolute scale using the corrected distances by X. Pang et al. (2021). We iteratively fit the polynomial by excluding points more than 0.4 mag away from the predicted value at each step until convergence. The formula is in the form

$$\hat{G}_{\rm abs} = \sum_{k=0}^{9} c_k \, (G_{\rm BP} - G_{\rm RP})^k, \tag{B1}$$

where $G_{BP} - G_{RP}$ is the Gaia DR3 color and $\hat{G}_{abs}$ the predicted Gaia DR3 absolute magnitude. The formula is valid in the range $-0.1126 < G_{BP} - G_{RP} < 3.5895$, but may not yield accurate results in the extreme blue end (due to a lack of samples) or the red end (due to M dwarfs that have not converged to the zero-age main sequence).

Table B1
Polynomial Coefficients for the Main Sequence of Blanco 1

Coefficient	Value
c_0	1.4827265
c_1	7.283127
c_2	−33.80652
c_3	99.9683
c_4	−138.4511
c_5	106.2048
c_6	−48.087944
c_7	12.809648
c_8	−1.8565603
c_9	0.11289064

Note. The coefficients are given up to eight decimal places not as significant figures but to reflect the machine precision of an IEEE 32-bit floating point number, which is the data type of Gaia magnitudes.

ORCID iDs

Lizhou Sha https://orcid.org/0000-0001-5401-8079
Andrew M. Vanderburg https://orcid.org/0000-0001-7246-5438
Luke G. Bouma https://orcid.org/0000-0002-0514-5538
Chelsea X. Huang https://orcid.org/0000-0003-0918-7484

References

Abril-Pla, O., Andreani, V., Carroll, C., et al. 2023, PeerJ Comp. Sci., 9, e1516
Aigrain, S., Hodgkin, S., Irwin, J., et al. 2007, MNRAS, 375, 29
Alfonso, J., & García-Varela, A. 2023, A&A, 677, A163
Anderson, E. R., Duvall, Thomas, L. J., & Jefferies, S. M. 1990, ApJ, 364, 699
Angus, R., Morton, T., Aigrain, S., Foreman-Mackey, D., & Rajpaul, V. 2018, MNRAS, 474, 2094
Astropy Collaboration, Price-Whelan, A. M., Lim, P. L., et al. 2022, ApJ, 935, 167
Astropy Collaboration, Price-Whelan, A. M., Sipőcz, B. M., et al. 2018, AJ, 156, 123
Astropy Collaboration, Robitaille, T. P., & Tollerud, E. J. 2013, A&A, 558, A33
Barber, M. G., Mann, A. W., Bush, J. L., et al. 2022, AJ, 164, 88
Barnes, S. A. 2003, ApJ, 586, 464
Barnes, S. A., Weingrill, J., Fritzewski, D., Strassmeier, K. G., & Platais, I. 2016, ApJ, 823, 16
Belokurov, V., Erkal, D., Evans, N. W., Koposov, S. E., & Deason, A. J. 2018, MNRAS, 478, 611
Bhatti, W., Bouma, L., & Yee, S. 2019, waqasbhatti/cdips-pipeline: cdips-pipeline, v0.1.0, Zenodo, doi:10.5281/zenodo.3370324
Blanco, V. M. 1949, PASP, 61, 183
Bouma, L. 2019, Cluster Difference Imaging Photometric Survey ("CDIPS"), STScI/MAST, doi:10.17909/T9-AYD0-K727
Bouma, L. G., Curtis, J. L., Hartman, J. D., Winn, J. N., & Bakos, G. Á 2021, AJ, 162, 197
Bouma, L. G., Hartman, J. D., Bhatti, W., Winn, J. N., & Bakos, G. Á 2019, ApJS, 245, 13
Bouma, L. G., Palumbo, E. K., & Hillenbrand, L. A. 2023, ApJL, 947, L3
Boyajian, T. S., von Braun, K., van Belle, G., et al. 2012, ApJ, 757, 112
Boyle, A. W., & Bouma, L. G. 2023, AJ, 166, 14
Brewer, J. M., Fischer, D. A., Valenti, J. A., & Piskunov, N. 2016, ApJS, 225, 32
Cantat-Gaudin, T., Jordi, C., Vallenari, A., et al. 2018, A&A, 618, A93
Cargile, P. A., James, D. J., & Jeffries, R. D. 2010, ApJL, 725, L111
Cargile, P. A., James, D. J., Pepper, J., et al. 2014, ApJ, 782, 29
Curtis, J. L., Agüeros, M. A., Mamajek, E. E., Wright, J. T., & Cummings, J. D. 2019, AJ, 158, 77
Curtis, J. L., Agüeros, M. A., Matt, S. P., et al. 2020, ApJ, 904, 140
Curtis, J. L., Vanderburg, A., Torres, G., et al. 2018, AJ, 155, 173
Dai, Y.-Z., Liu, H.-G., Yang, J.-Y., & Zhou, J.-L. 2023, AJ, 166, 219
Delorme, P., Collier Cameron, A., Hebb, L., et al. 2011, MNRAS, 413, 2218
Douglas, S. T., Agüeros, M. A., Covey, K. R., et al. 2016, ApJ, 822, 47
Duane, S., Kennedy, A. D., Pendleton, B. J., & Roweth, D. 1987, PhLB, 195, 216
Esselstein, R., Aigrain, S., Vanderburg, A., et al. 2018, ApJ, 859, 167
Evans, D. W., Riello, M., De Angeli, F., et al. 2018, A&A, 616, A4
Foreman-Mackey, D. 2018, RNAAS, 2, 31
Foreman-Mackey, D., Agol, E., Ambikasaran, S., & Angus, R. 2017, AJ, 154, 220
Gagné, J. 2024, PASP, 136, 063001
Gagné, J., Faherty, J. K., Moranta, L., & Popinchalk, M. 2021, ApJL, 915, L29
Gagné, J., Mamajek, E. E., Malo, L., et al. 2018, ApJ, 856, 23
Gaia Collaboration, Babusiaux, C., van Leeuwen, F., et al. 2018a, A&A, 616, A10
Gaia Collaboration, Brown, A. G. A., & Vallenari, A. 2018b, A&A, 616, A1
Gaia Collaboration, Prusti, T., de Bruijne, J. H. J., et al. 2016, A&A, 595, A1
Gillen, E., Briegal, J. T., Hodgkin, S. T., et al. 2020, MNRAS, 492, 1008
Ginsburg, A., Sipőcz, B. M., Brasseur, C. E., et al. 2019, AJ, 157, 98
Górski, K. M., Hivon, E., Banday, A. J., et al. 2005, ApJ, 622, 759
Harris, C. R., Millman, K. J., van der Walt, S. J., et al. 2020, Natur, 585, 357
Hartman, J. D., Bakos, G. Á, Kovacs, G., & Noyes, R. W. 2010, MNRAS, 408, 475
He, Z., Wang, K., Luo, Y., et al. 2022, ApJS, 262, 7
Hodgkin, S. T., Harrison, D. L., Breedt, E., et al. 2021, A&A, 652, A76
Hoffman, M. D., & Gelman, A. 2014, JMLR, 15, 1593
Hunt, E. L., & Reffert, S. 2021, A&A, 646, A104
Hunt, E. L., & Reffert, S. 2023, A&A, 673, A114
Hunter, J. D. 2007, CSE, 9, 90
Irwin, J., Aigrain, S., Bouvier, J., et al. 2009, MNRAS, 392, 1456
Ivezic, Ž., Connolly, A. J., VanderPlas, J. T., & Gray, A. 2014, Statistics, Data Mining, and Machine Learning in Astronomy: A Practical Python Guide for the Analysis of Survey Data (Princeton, NJ: Princeton Univ. Press)
Jerabkova, T., Boffin, H. M. J., Beccari, G., et al. 2021, A&A, 647, A137
Kounkel, M., & Covey, K. 2019, AJ, 158, 122
Kounkel, M., Covey, K., & Stassun, K. G. 2020, AJ, 160, 279
Krumholz, M. R., McKee, C. F., & Bland-Hawthorn, J. 2019, ARA&A, 57, 227
Kupper, A. H. W., Macleod, A., & Heggie, D. C. 2008, MNRAS, 387, 1248
Lada, C. J., & Lada, E. A. 2003, ARA&A, 41, 57
Li, Y., Pang, X., & Tang, S.-Y. 2021, RNAAS, 5, 173
Lindegren, L., Klioner, S. A., Hernández, J., et al. 2021, A&A, 649, A2
Lomb, N. R. 1976, Ap&SS, 39, 447
Mann, A. W., Feiden, G. A., Gaidos, E., Boyajian, T., & von Braun, K. 2015, ApJ, 804, 64
Matplotlib Development Team 2023, Matplotlib: Visualization with Python, v3.8.2, Zenodo, doi:10.5281/zenodo.10150955
McKinney, W. 2010, in Proc. 9th Python in Science Conf., ed. S. van der Walt & J. Millman (Austin, TX: SciPy), 56
Meibom, S., Barnes, S. A., Latham, D. W., et al. 2011, ApJL, 733, L9
Meibom, S., Mathieu, R. D., & Stassun, K. G. 2007, ApJL, 665, L155
Meingast, S., Alves, J., & Fürnkranz, V. 2019, A&A, 622, L13
Meingast, S., Alves, J., & Rottensteiner, A. 2021, A&A, 645, A84

Newton, E. R., Rampalli, R., Kraus, A. L., et al. 2022, AJ, 164, 115
Paegert, M., Stassun, K. G., Collins, K. A., et al. 2021, arXiv:2108.04778
Pandas Development Team 2023, Pandas-dev/Pandas: Pandas, v2.1.4, Zenodo, doi:10.5281/zenodo.10304236
Pang, X., Li, Y., Yu, Z., et al. 2021, ApJ, 912, 162
Pepper, J., Kuhn, R. B., Siverd, R., James, D., & Stassun, K. 2012, PASP, 124, 230
Pepper, J., Stanek, K. Z., Pogge, R. W., et al. 2008, AJ, 135, 907
Rampalli, R., Agüeros, M. A., Curtis, J. L., et al. 2021, ApJ, 921, 167
Rebull, L. M., Stauffer, J. R., Bouvier, J., et al. 2016, AJ, 152, 113
Ricker, G. R., Winn, J. N., Vanderspek, R., et al. 2015, JATIS, 1, 014003
Salvatier, J., Wiecki, T., & Fonnesbeck, C. 2015, arXiv:1507.08050
Scargle, J. D. 1982, ApJ, 263, 835
Soderblom, D. R., Hillenbrand, L. A., Jeffries, R. D., Mamajek, E. E., & Naylor, T. 2014, in Protostars and Planets VI, ed. H. Beuther et al. (Tucson, AZ: Univ. Arizona Press), 219
Stassun, K. G., Oelkers, R. J., Paegert, M., et al. 2019, AJ, 158, 138
Tarricq, Y., Soubiran, C., Casamiquela, L., et al. 2022, A&A, 659, A59
Tofflemire, B. M., Rizzuto, A. C., Newton, E. R., et al. 2021, AJ, 161, 171
VanderPlas, J. T. 2018, ApJS, 236, 16
Virtanen, P., Gommers, R., Oliphant, T. E., et al. 2020, NatMe, 17, 261
Zhang, Y., Tang, S.-Y., Chen, W. P., Pang, X., & Liu, J. Z. 2020, ApJ, 889, 99